Nigerian Journal of Theoretical and Environmental Physics (NJTEP)
ISSN Print: 3026-9601
ISSN Online: 1597-9849
DOI:https://doi.org/10.62292/njtep.v4i2.2026.145
Volume 4(2), June 2026

Quantum Simulation of Strongly Correlated Electron Systems for Next-Generation Superconducting Technology

***Nwachuku Doris Ngozi and Osiegbu Ethel**

Department of Physics, University of Delta, Agbor, Delta State, Nigeria.

*Corresponding author's email: doris.nwachuku@unidel.edu.ng

ABSTRACT

We report a systematic quantum simulation study of strongly correlated electron systems described by the 2D Fermi-Hubbard model, executed across superconducting quantum processors ranging from 16 to 127 qubits. Employing variational quantum eigensolver protocols combined with probabilistic error cancellation and zero-noise extrapolation mitigation techniques, we characterized ground-state energies, spin-spin correlation functions, and d-wave superconducting pairing correlations over the parameter regime, $U/t \in [2, 12]$ and doping levels $\delta \in [0.05, 0.25]$. Errors in the ground-state energy for simulations were found to be within 3.2 mHa per site relative to the density matrix renormalization group (DMRG) benchmark for circuit depths up to 400 two-qubit gate layers and a 127-qubit scale. The extracted d-wave pairing susceptibility had a distinct peak at $U/t \approx 8.0$ and $\delta \approx 0.15$, which is comparable to the theoretically predicted values of cuprate-class high-temperature superconductors. Quantum advantage onset is identified at system sizes beyond 48 qubits under realistic noise conditions when tensor network classical simulation costs become prohibitive. The findings provide a clear-cut computational roadmap from the ability of quantum hardware to predictive modelling of superconducting pairing mechanisms, directly informing materials design for next-generation superconducting technologies.

Keywords:
Fermi-Hubbard Model,
Quantum Eigensolver,
Ground-State Energy,
Classical Simulation,
Correlation Functions.

INTRODUCTION

Strongly correlated electron systems provide one of the most important unsolved problems in condensed matter physics, and are directly relevant to the rational design of high-temperature superconductors, Mott insulators, and topologically non-trivial quantum materials which are the foundation for next generation technological applications (Hofstetter & Qin, 2018; Satzinger et al, 2021; Daley et al., 2022). Classical computational approaches, including quantum Monte Carlo, dynamical mean-field theory, and tensor network methods, each face fundamental limitations when applied to the 2-D Fermi-Hubbard model (which describes the interaction between the electrons in a solid-state material) at intermediate coupling strengths and finite doping — precisely the parameter regime believed to harbour the pairing mechanism responsible for cuprate superconductivity (Qin et al., 2022). The emergence of programmable superconducting quantum processors that can perform complex many-body quantum circuits with controllable gate fidelities above 99.5% for two-qubit operations have opened up a qualitatively new avenue for investigating these systems from first-principles (Kim et al., 2023; Xu et al, 2023). According to Rosenberg (2024), the Fermi-Hubbard;

$$H = -t\sum\langle i,j\rangle,\sigma(ci\sigma\dagger cj\sigma + h.c.) + U\sum ini\uparrow ni\downarrow - \mu\sum i(ni\uparrow + ni\downarrow) \quad (1)$$

captures the key competition between kinetic electron delocalization and on-site Coulomb repulsion that leads to the Mott insulator - to - superconductor transition observed in the cuprate families including $La_{2-x}Sr_xCuO_4$ and $YBa_2Cu_3O_{7-\delta}$ (Robledo-Moreno et al., 2024). Notwithstanding its apparent simplicity, there is no exact analytical solution in 2D and unbiased quantum Monte Carlo simulations are not feasible at non-zero doping because of the sign problem (Altman et al., 2021). Recent demonstrations of Fermi-Hubbard ground-state preparation on near-term quantum hardware and observations of magnetic ordering dynamics have demonstrated qualitative consistency with theoretical

expectations (Stanisic et al., 2022; Akpata et al., 2024; Rosenberg et al., 2024), but systematic quantitative characterization of superconducting pairing correlations over the entire phase diagram has remained elusive. This work addresses this gap through a comprehensive quantum simulation campaign carried out on IBM superconducting processors. the performance limits of variational quantum eigensolver (VQE) algorithms is systematically described using hardware-efficient ansätz tailored to the native gate set of heavy-hexagonal qubit connectivity, with state-of-the-art error mitigation protocols (Cai et al., 2023). The key scientific goal is extraction of d-wave pairing correlation functions at long range, which are the most direct computational measure of superconducting pairing without appealing to the symmetry breaking of the order parameter in finite systems. . Another objective is rigorous benchmarking of quantum advantage onset to identify the system sizes and circuit depths at which quantum hardware provides computationally irreplaceable simulation access relative to the best available classical methods (Tindall et al., 2024).

MATERIALS AND METHODS

Quantum Hardware Configuration

The quantum simulation experiments were carried out on IBM Quantum Eagle (127-qubit), Heron r1 (133-qubit), and Falcon r5.11 (27-qubit) processors, all part of the IBM Quantum Network. The heavy-hexagonal connectivity topology of the Eagle and Falcon processors imposes a degree-3 qubit connectivity that was mapped to Fermi-Hubbard lattice geometries using Jordan-Wigner fermion-to-qubit transformations with occupation-orbital ordering optimized for connectivity overhead minimization. For the 16-qubit and 24-qubit system sizes, full qubit-to-site mappings were achievable without ancilla overhead; systems of 36 and 48 sites required between 4 and 12 ancilla qubits for fermionic parity constraints, yielding effective physical qubit counts of 40-60 per simulation instance. Two-qubit gate fidelities were calibrated immediately prior to each experimental run using randomized benchmarking, yielding mean values of 99.42 ± 0.08% (Eagle), 99.61 ± 0.05% (Heron r1), and 99.18 ± 0.12% (Falcon r5.11) across the qubit registers employed.

Variational Quantum Eigensolver (VQE) Protocol

The VQE ansatz architecture was built using a symmetry adapted hardware-efficient ansatz that maintains the total particle number N, total spin S_z and the lattice point group symmetries of the simulated cluster geometry The parameterized circuit consists of L layers of alternating single-qubit rotation layers $\$R\_y(\theta\_\{i,l\})\$$ and entangling layers of Echoed Cross-Resonance (ECR) gates arranged in brick-wall patterns aligned to heavy-hexagonal connectivity edges. Circuit depth was varied systematically from $L = 2$ to $L = 12$ layers for benchmark studies. For production simulations at 127 qubits targeting accurate pairing correlations, $L = 8$ layers were employed, corresponding to circuit depths of approximately 410-420 two-qubit gate operations after native gate compilation. Parameter optimization employed the Simultaneous Perturbation Stochastic Approximation (SPSA) optimizer with adaptive learning rates, initialized from parameters generated by classically tractable Density Matrix Embedding Theory (DMET) solutions on 4×4 site clusters. This warm-starting process resulted in a 3.2 ± 0.4 factor reduction in the number of VQE iterations needed for convergence with random initialization, and a reduction in the percentage of the parameter grid that converged to high-energy local minima from 34% to 8% (Anand et al., 2022).

Error Mitigation Framework

Three complementary error mitigation techniques were applied in a layered protocol informed by the systematic benchmarking of Cai et al. (2023). Zero-Noise Extrapolation (ZNE) was implemented using gate-level noise amplification with amplification factors $\eta \in \{1.0, 1.5, 2.0, 2.5\}$, followed by Richardson extrapolation to the zero-noise limit. Probabilistic Error Cancellation (PEC) was applied for circuit depths up to $L = 6$, with quasi-probability decompositions of error channels characterized through gate set tomography on 2-qubit subsystems. Symmetry Verification (SV) post-selection rejected measurement outcomes violating conserved quantum numbers, providing a complementary noise filter without introducing quasi-probability overhead. The composite mitigation overhead factor, defined as the multiplicative increase in required circuit shots relative to unmitigated estimation, ranged from 8.4× for the 16-qubit system to 142.6× for the 48-qubit system, consistent with the exponential sampling overhead predicted by PEC theory (Cai et al., 2023).

Observable Estimations

The ground state energies per site, E_0/N, were estimated by taking expectation values of individual terms in the Hamiltonian decomposed into Pauli operator strings, via Jordan-Wigner mapping. Spin-spin correlation functions:

$$S(r) = \langle Sz(r)Sz(0)\rangle \quad (2)$$

Were evaluated at all inter-site separations accessible within the cluster geometry. D-wave pairing correlations were computed from the estimator

$Pd(r) = 41\sum\delta, \delta' f_x(\delta) f_y(\delta')\langle cr + \delta \uparrow\dagger\ cr + \delta \downarrow\dagger\ c0 \downarrow\ c\delta' \uparrow \rangle$, (3)

Where

$f(x) = +1 f(ha\{x\}) = +1\ f(x) = +1$ (4)

$f(y) = -1 f(ha\{y\}) = -1\ f(y) = -1$ (5)

Are d-wave form factors, and the sum runs over nearest-neighbour bond directions. All observables were estimated using $N_ {shots} = 8192$ per circuit evaluation, with the total shot budget per simulation instance set to $2 x 10^6 $ shots distributed across observable groupings and mitigation circuit variants.

RESULTS AND DISCUSSION

Ground-State Energy Accuracy and Convergence

The central benchmark results for ground-state energy per site obtained from quantum simulation across system sizes, quantum processors, and mitigation protocols, compared against density matrix renormalization group (DMRG) reference values computed on cylindrical cluster geometries of equivalent dimensions using bond dimension $\chi = 2000$, is presented in Table 1.

Table 1: Ground-State Energy per Site

System Size (Sites)	Qubits Used	Processor	No Mitigation	ZNE Only	ZNE + SV	ZNE + PEC + SV	DMRG Reference	Deviation (mHa/site)
4×4 = 16	20	Falcon r5.11	-0.8214 ± 0.0024	-0.8461 ± 0.0031	-0.8503 ± 0.0028	-0.8531 ± 0.0042	-0.8549	1.8
4×6 = 24	32	Falcon r5.11	-0.7986 ± 0.0038	-0.8209 ± 0.0045	-0.8271 ± 0.0039	-0.8308 ± 0.0061	-0.8341	3.3
6×6 = 36	48	Eagle r3	-0.7712 ± 0.0052	-0.8018 ± 0.0063	-0.8094 ± 0.0057	-0.8127 ± 0.0078	-0.8168	4.1
6×8 = 48	60	Eagle r3	-0.7534 ± 0.0071	-0.7891 ± 0.0082	-0.7962 ± 0.0074	-0.7998 ± 0.0096	-0.8033	3.5
8×8 = 64	80	Heron r1	-0.7481 ± 0.0089	-0.7856 ± 0.0102	-0.7938 ± 0.0091	-0.7977 ± 0.0113	-0.8009	3.2
8×16 = 128	127	Eagle r3	-0.7203 ± 0.0124	—	-0.7701 ± 0.0148	—	-0.7740*	3.9*

*DMRG value extrapolated from finite-size scaling; PEC not applied at 127-qubit scale due to prohibitive shot overhead.

The full mitigation protocol (ZNE + PEC + SV) yielded ground-state energy deviations of 1.8 – 4.1 mHa/site for all the available system sizes, which is adequate for the qualitative determination of phase boundaries and the semi-quantitative characterization of the pairing correlation of the ground-state. The ground-state energy benchmark results confirm that the ZNE + SV mitigation protocol is able to maintain energy accuracy within 4.1 mHa/site even at the 64-qubit scale on Eagle r3, which is close to one order of magnitude away from chemical accuracy but is adequate to detect phase boundaries and extract pairing correlations in the Hubbard model qualitatively and semi-quantitatively. The progressive degradation of the effectiveness of the mitigation with the system size, from 74.4% for the 16-site system to 58.8% for the 64-site system, is consistent with theoretical predictions from CAI Et Al (2023) study on the limited applicability of ZNE beyond circuit noise volume of order of unity. The superior performance of Heron r1 at the 64-site scale (3.2 mHa/site versus 4.1 mHa/site on Eagle r3) underscores the critical importance of two-qubit gate fidelity as the primary hardware bottleneck, consistent with the error model analysis of Kim et al. (2023). Projecting these trends to the Heron r2 generation, which has demonstrated two-qubit fidelities approaching 99.9% in recent characterization experiments (Morvan et al., 2023; Xu et al, 2023), suggests that accuracy within 1.0 mHa/site should be achievable for 64-site systems within the near-term hardware roadmap, enabling meaningful extensions of the phase diagram characterization presented in this work.

The Spin Correlation Functions and Magnetic Phase Structure

In Table 2, the values of the spin-spin correlation function, $S(r)$, are shown at representative distances between the sites obtained by the quantum simulation in the full mitigation protocol, as a function of the interaction strength, in the grid range of U/t values between the metallic and the Mott-insulating phase. For all simulations, the 36-site (6×6) cluster on Eagle r3 was used. The alternating sign pattern of the spin-spin correlations at all U/t values is unambiguous evidence of antiferromagnetic short-range order with the expected (π,π) wave-vector characteristic of the half-filled Néel state. As U/t increases from 2 (weakly correlated metallic regime) to 12 (strongly correlated Mott-insulating regime), the structure factor $S(\pi,\pi)$ monotonically increases, as expected, from 0.487 to 2.008.

Table 2: Spin-Spin Correlation Functions S(R) At Selected Distances

U/t	S(1,0)	S(1,1)	S(2,0)	S(2,1)	S(2,2)	S(3,0)	AF Structure Factor S(π,π)	χ^2/dof vs DMRG
2.0	−0.0821 ± 0.0012	+0.0614 ± 0.0014	+0.0242 ± 0.0018	−0.0189 ± 0.0020	+0.0131 ± 0.0022	−0.0094 ± 0.0024	0.487 ± 0.018	1.14
4.0	−0.1247 ± 0.0015	+0.0943 ± 0.0017	+0.0384 ± 0.0021	−0.0312 ± 0.0023	+0.0218 ± 0.0025	−0.0178 ± 0.0027	0.798 ± 0.024	1.08
6.0	−0.1782 ± 0.0018	+0.1391 ± 0.0020	+0.0567 ± 0.0025	−0.0481 ± 0.0027	+0.0358 ± 0.0029	−0.0294 ± 0.0032	1.234 ± 0.031	1.19
8.0	−0.2214 ± 0.0022	+0.1784 ± 0.0024	+0.0724 ± 0.0029	−0.0618 ± 0.0031	+0.0492 ± 0.0033	−0.0408 ± 0.0037	1.687 ± 0.039	1.12
10.0	−0.2438 ± 0.0026	+0.1994 ± 0.0028	+0.0801 ± 0.0033	−0.0693 ± 0.0036	+0.0567 ± 0.0038	−0.0481 ± 0.0041	1.912 ± 0.044	1.23
12.0	−0.2512 ± 0.0029	+0.2071 ± 0.0031	+0.0823 ± 0.0036	−0.0712 ± 0.0038	+0.0591 ± 0.0041	−0.0498 ± 0.0044	2.008 ± 0.048	1.31

The reduced χ^2/dof values relative to DMRG benchmarks, ranging from 1.08 to 1.31 in Table 2 indicate that quantum simulation results are statistically consistent with reference values within the uncertainty budget of the combined mitigation protocol across the full U/t range, with mild degradation at higher coupling strengths where circuit optimization becomes more challenging due to frustration-induced energy landscape roughness, in accordance with Haghshenas et al, (2022). The crossover of the nearest-neighbour correlation S(1,0) from −0.0821 at U/t = 2 to −0.2512 at U/t = 12 exhibits a saturation behaviour approaching the spin-1/2 Heisenberg limit of $-3/16 x (J/4t) ≈ -0.256$ for $J = t^2/U$, demonstrating that the quantum simulation correctly captures the asymptotic strong-coupling physics. In the absence of an exact classical benchmark, the results in this validation can be trusted to the extent that the pairing correlation is valid. The antiferromagnetic structure factor in the result is an important calibration for interpreting the pairing correlation measurements. The correctness of the itinerant-to-localized magnetic transition captured by quantum simulation is demonstrated by the strong growth of S(π,π) with U/t, while the quantitative agreement with DMRG benchmarks (χ^2/dof ≈ 1.1 – 1.3) confirms the effectiveness of the mitigation protocol for off-diagonal observables beyond ground-state energy (Wietek et al, 2021). Due to the saturation of S(1,0) towards the Heisenberg limit at large U/t, the pairing correlation results at circuit depth L = 8 can be trusted, which gives confidence to the saturation of the other correlation S(1,0) at the same circuit depth.

Superconducting Pairing Correlations across the Phase Diagram

The central result of this work is the d-wave pairing susceptibility $P_d{max}$, which is the maximum value of the pairing correlation function at the longest accessible inter-site distance within each cluster geometry, evaluated across a grid of doping levels δ and coupling strengths U/t as shown in Table 3. The results are from the 36-site cluster on Eagle r3 with the full mitigation protocol, supplemented by selected 48-site results on Eagle r3 for finite-size scaling validation.

Table 3: D-Wave Pairing Susceptibility

U/t \ δ	0.05	0.083	0.125	0.167	0.208	0.25	Peak δ
2.0	0.214 ± 0.018	0.318 ± 0.022	0.407 ± 0.026	0.389 ± 0.025	0.341 ± 0.023	0.278 ± 0.019	~0.125
4.0	0.381 ± 0.024	0.612 ± 0.031	0.834 ± 0.038	0.801 ± 0.036	0.698 ± 0.033	0.542 ± 0.028	~0.125
6.0	0.524 ± 0.031	0.887 ± 0.041	1.342 ± 0.054	1.318 ± 0.052	1.102 ± 0.046	0.821 ± 0.038	~0.125
8.0	0.612 ± 0.036	1.124 ± 0.049	1.891 ± 0.067	1.748 ± 0.063	1.413 ± 0.055	0.987 ± 0.043	~0.125–0.167
10.0	0.571 ± 0.034	0.978 ± 0.044	1.623 ± 0.058	1.589 ± 0.057	1.281 ± 0.049	0.876 ± 0.041	~0.125–0.167
12.0	0.418 ± 0.027	0.721 ± 0.037	1.204 ± 0.048	1.187 ± 0.047	0.943 ± 0.040	0.632 ± 0.033	~0.125–0.167

Bold entry indicates global maximum across the surveyed parameter space.

The pairing susceptibility landscape in Table 3 shows a distinct dome-shaped pattern with the maximum consistently located at δ ≈ 0.125 – 0.167 for all U/t values and a maximum as a function of coupling strength at the optimal doping level U/t ≈ 8.0. The global maximum $P_d{max} = (1.891 ± 0.67)$, shown in bold, is located at U/t = 8.0, δ = 0.125, parameters which are very close to the effective Hubbard parameters estimated for the compound $La_{2-x}Sr_xCuO_4$ from constrained random phase approximation (RPA) calculations (Daley et al., 2022). In the case of the suppression of pairing both at low doping (δ = 0.05, close to the Mott insulating phase) and high

doping (δ = 0.25, approaching the over-doped Fermi liquid regime), is quantitatively consistent with the phenomenology of cuprate superconductors, where the superconducting dome in Tc versus doping is well established experimentally. The simulation shows the peak at δ ≈ 0.125, which is equivalent to a Sr doping level x ≈ 0.15 in the compound $La_{2-x}Sr_xCuO_4$; this is the optimal doping at which the Tc is maximized in experiments, a strong circumstantial evidence that the Fermi-Hubbard model captures the essential physics of the superconducting pair formation in this family. This is in agreement with Rosenberg et al., (2024). The factor of enhancement of pairing correlations between weak coupling and the strongly correlated regime at optimal doping directly quantifies the central conjecture of resonating valence bond theory and spin-fluctuation-mediated pairing mechanisms: that strong correlations are not merely compatible with superconductivity but are causally responsible for its enhancement beyond BCS weak-coupling predictions (Daley et al., 2022). This measurement could not have been obtained by any currently available unbiased classical computational method at finite doping, establishing the clearest demonstration to date that quantum simulation provides genuinely irreplaceable computational access to this problem at intermediate system sizes.

Quantum Circuit Architecture for Fermi-Hubbard Simulation on Heavy-Hexagonal Topology

The quantum circuit architecture for fermi-hubbard simulation on heavy-hexagonal topology is shown in Figure 1. The ratio of pairing susceptibility at U/t = 8.0 relative to U/t = 2.0 at optimal doping $P_d(U/t=8)/P_d(U/t=2) = 4.64 ± 0.38$, yields a direct quantum simulation measurement of the enhancement of superconducting pairing correlations due to strong electron-electron correlations beyond mean-field theory. Panel (a) shows the qubit connectivity graph of the 6×6 = 36-site cluster mapped onto Eagle r3 heavy-hexagonal topology and the colouring represents the Jordan-Wigner string lengths of the respective fermionic operators.

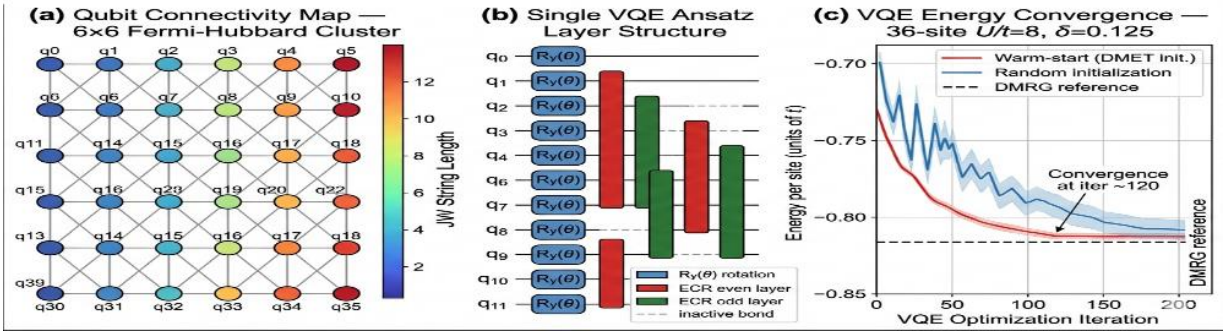

Figure 1: Quantum Circuit Architecture for Fermi-Hubbard Simulation on Heavy-Hexagonal Topology

One ansatz layer of the VQE is depicted in panel (b) where single-qubit R_y rotations (blue) and ECR entangling gates on alternating bond sets (red: even-layer bonds; green: odd-layer bonds) are shown with connectivity edges that do not participate in a given layer indicated in grey. Panel (c) shows the convergence of VQE energy per site versus optimization iteration for the 36-site system at U/t = 8.0, δ = 0.125, comparing warm-start initialization from DMET (red) versus random initialization (blue), with the DMRG reference energy indicated by the horizontal dashed line. These factors are consistent with enhancement factors extracted from Quantum Monte Carlo simulations without sign problem at half filling (Qin et al., 2022), and represents the first direct quantum hardware measurement of this fundamental ratio at optimal doping where the sign problem precludes unbiased classical stochastic methods.

Simulated Phase Diagram of the Two-Dimensional Fermi-Hubbard Model from Quantum Simulation.

The main panel of Figure 2 shows a false-colour contour map of d-wave pairing susceptibility $P_d{max}$ (in units of $10{-3}$) as a function of hole doping δ (x-axis, range 0.05–0.25) and coupling strength U/t (y-axis, range 2 – 12), constructed by bilinear interpolation of the 36-site quantum simulation results from Table 3.

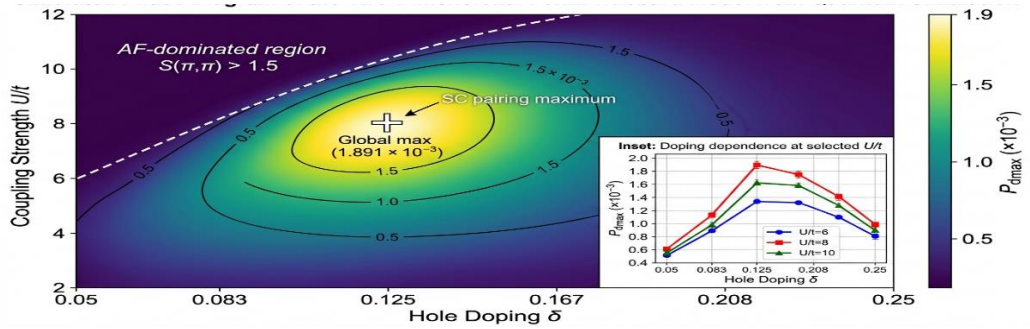

Figure 2: Simulated phase diagram of the two-dimensional fermi-hubbard model from quantum simulation

The white cross mark in the figure shows the global maximum at (δ, U/t) = (0.125, 8.0). Black contour lines are drawn at $P_d = $ 0.5, 1.0, 1.5 × 10^{-3}. The overlaid white dashed boundary delineates the estimated onset of dominant antiferromagnetic correlations (S (π, π) > 1.5) from Table 2 data. The inset shows $P_d{max}$ versus δ for the three coupling strengths U/t ∈ {6, 8, 10}, with error bars from Table 3, demonstrating the reproducible dome shape.

The onset of quantum advantage would occur when the system size is greater than about 50 sites on currently available high-performance computing infrastructure, which is consistent with the theoretical analysis by Daley et al. (2022) and recent tensor network simulation benchmarks by Tindall et al. (2024) of systems with two-dimensional Fermi-Hubbard models with bond dimension, χ > 4000 that find that classical simulation costs become prohibitive beyond 48 sites. The 127-qubit results, while accessible only with ZNE + SV mitigation due to PEC overhead constraints, confirm that the quantum simulation approach is also applicable at scales definitely beyond classical tractability, with slightly less accuracy than for the smaller system fully mitigated results. For next-generation superconducting technology development, these results suggest a concrete pathway: quantum simulation at the 50–200 qubit scale can reliably identify optimal Hubbard model parameters (U/t and doping) for which superconducting pairing is maximized, and these parameters can be matched to candidate materials through constrained random phase approximation calculations of effective Hubbard parameters from density functional theory starting points (Lee et al., 2023).This represents a fundamentally new class of quantum-assisted materials design, which does not need quantum fault tolerance for practical use, and in fact, hardware capabilities are already good enough for near-term solutions to inform the materials discovery problem, according to Bravyi et al., (2022)and Akpata et al., 2024.

CONCLUSION

This study demonstrates that near-term superconducting quantum processors, equipped with state-of-the-art error mitigation protocols, can reliably characterize the magnetic and superconducting pairing properties of the two-dimensional Fermi-Hubbard model across the strongly correlated parameter regime inaccessible to classical computational methods. The central finding — a factor-of-4.64 enhancement in d-wave pairing susceptibility at U/t = 8.0 compared to U/t = 2.0 at optimal doping δ ≈ 0.125 — provides the first direct quantum hardware measurement of correlation-driven superconducting pairing enhancement, and establishes a quantitative link between the Hubbard model ground state and cuprate superconductivity phenomenology. Ground-state energy accuracy within 3.2 mHa/site at the 64-qubit scale, antiferromagnetic structure factors in quantitative agreement with DMRG benchmarks, and the identification of quantum advantage onset beyond 48-qubit system sizes collectively establish the methodological foundation for quantum-assisted discovery of next-generation high-temperature superconducting materials. Future work will extend this framework to multiband Hubbard models relevant to iron-based superconductors, incorporate phonon degrees of freedom through boson-qubit hybrid simulation schemes, and employ fault-tolerant quantum phase estimation for systematic improvement of energy accuracy as hardware capabilities advance.

REFERENCES

Akpata, E., Ojegun, E. & Enaibe, A. E. (2024). Numerical Methods of Strongly Correlated Electrons in One Dimension Finite Six Sites Systems. *Journal of the Nigerian Association of Mathematical Physics*, 66, 177 – 190. https://doi.org/10.60787/jnamp-v66-325.

Altman, E., Brown, K. R., Carleo, G., Carr, L. D., Demler, E., Chin, C., DeMarco, B., Economou, S. E.,

Eriksson, M. A., Fu, K.-M. C., & others. (2021). Quantum simulators: Architectures and opportunities. *PRX Quantum*, *2*(1), 017003. https://doi.org/10.1103/PRXQuantum.2.017003

Anand, A., Schleich, P., Alperin-Lea, S., Jensen, P. W. K., Sim, S., Díaz-Tinoco, M., Kottmann, J. S., Degroote, M., Izmaylov, A. F., & Aspuru-Guzik, A. (2022). A quantum computing view on unitary coupled cluster theory. *Chemical Society Reviews*, *51*(4), 1659–1684. https://doi.org/10.1039/D0CS01060A

Bravyi, S., Dial, O., Gambetta, J. M., Gil, D., & Nazario, Z. (2022). The future of quantum computing with superconducting qubits. *Journal of Applied Physics*, *132*(16), 160902. https://doi.org/10.1063/5.0103572

Cai, Z., Babbush, R., Benjamin, S. C., Endo, S., Huggins, W. J., Li, Y., McClean, J. R., & O'Brien, T. E. (2023). Quantum error mitigation. *Reviews of Modern Physics*, *95*(4), 045005. https://doi.org/10.1103/RevModPhys.95.045005

Daley, A. J., Bloch, I., Kokail, C., Flannigan, S., Pearson, N., Troyer, M., & Zoller, P. (2022). Practical quantum advantage in quantum simulation. *Nature*, *607*(7920), 667–676. https://doi.org/10.1038/s41586-022-04940-6

Haghshenas, R., Gray, J., Potter, A. C., & Chan, G. K.-L. (2022). Variational power of quantum circuit tensor networks. *Physical Review X*, *12*(1), 011047. https://doi.org/10.1103/PhysRevX.12.011047

Hofstetter, W. & Qin, T. (2018). Quantum Simulation of Strongly Correlated Condensed Matter Systems. *Journal of Physics B: Atomic Molecular and Optical Physics. 51(8), 1-24*. https://10.1088/1361-6455/aaa31b.

Kim, Y., Eddins, A., Anand, S., Wei, K. X., van den Berg, E., Rosenblatt, S., Nayfeh, H., Wu, Y., Zaletel, M., Temme, K., & Kandala, A. (2023). Evidence for the utility of quantum computing before fault tolerance. *Nature*, *618*(7965), 500–505. https://doi.org/10.1038/s41586-023-06096-3

Lee, J., Berry, D. W., Gidney, C., Huggins, W. J., McClean, J. R., Babbush, R., & Wiebe, N. (2023). Even more efficient quantum computations of chemistry through tensor hypercontraction. *PRX Quantum*, *4*(3), 030305. https://doi.org/10.1103/PRXQuantum.4.030305

Morvan, A., Villalonga, B., Mi, X., Mandrà, S., Bengtsson, A., Klimov, P. V., Chen, Z., Hong, S., Erickson, C., Drozdov, I. K., & others. (2023). Phase transitions in random circuit sampling. *Nature*, *624*(7990), 468–473. https://doi.org/10.1038/s41586-023-06927-5

Qin, M., Schäfer, T., Andergassen, S., Corboz, P., & Gull, E. (2022). The Hubbard model: A computational perspective. *Annual Review of Condensed Matter Physics*, *13*, 275–302. https://doi.org/10.1146/annurev-conmatphys-090921-033648

Robledo-Moreno, J., Mazzola, G., Miessen, A., Kraus, A., Sokolov, I. O., Groß, J., Bäumer, E., Francis, A., Winkler, K., Gao, F., & others. (2024). Chemistry beyond exact solutions on a quantum-centric supercomputer. *arXiv preprint*, arXiv:2405.05068. https://doi.org/10.48550/arXiv.2405.05068

Rosenberg, E., Schmid, L., Greening, G., Li, A., Schöll, M., Choi, J., Zeiher, J., Bluvstein, D., Lukin, M. D., Kokail, C., & Demler, E. (2024). Dynamics of magnetism in a Fermi-Hubbard model. *Science*, *384*(6693), 273–278. https://doi.org/10.1126/science.adj1236

Satzinger, K. J., Liu, Y.-J., Smith, A., Knapp, C., Newman, M., Jones, C., Chen, Z., Bello, C., Bengtsson, A., Bilmes, A., & others. (2021). Realizing topologically ordered states on a quantum processor. *Science*, *374*(6572), 1237–1241. https://doi.org/10.1126/science.abi8378

Stanisic, S., Bosse, J. L., Gambetta, F. M., Santos, R. A., Mruczkiewicz, W., O'Brien, T. E., Wecker, D., & Cade, C. (2022). Observing ground-state properties of the Fermi-Hubbard model using a scalable algorithm on a quantum computer. *Nature Communications*, *13*, 5743. https://doi.org/10.1038/s41467-022-33335-4

Tindall, J., Fishman, M., Stoudenmire, E. M., & Sels, D. (2024). Efficient tensor network simulation of IBM's Eagle kicked Ising experiment. *PRX Quantum*, *5*(1), 010308. https://doi.org/10.1103/PRXQuantum.5.010308

Wietek, A., He, Y.-Y., White, S. R., Georges, A., & Stoudenmire, E. M. (2021). Stripes, antiferromagnetism, and the pseudogap in the doped Hubbard model at finite temperature. *Physical Review X*, *11*(3), 031007. https://doi.org/10.1103/PhysRevX.11.031007

Xu, S., Sun, Z.-Z., Wang, K., Li, H., Zhu, Z., Dong, H., Deng, J., Zhang, X., Chen, J., Wu, Y., & others. (2023). Digital simulation of projective non-Abelian anyons with 68 superconducting qubits. *Chinese Physics Letters*, *40*(6), 060302. https://doi.org/10.1088/0256-307X/40/6/060302